

Atomistic evaluation of tension-compression asymmetry in nanoscale body-centered-cubic AlCrFeCoNi high-entropy alloy

Runlong Xing(邢润龙) and Xuepeng Liu(刘雪鹏)
Citation: Chin. Phys. B, 2024, 33 (**1**): 016202. DOI: 10.1088/1674-1056/acfc37
Journal homepage: http://cpb.iphy.ac.cn; http://iopscience.iop.org/cpb

What follows is a list of articles you may be interested in

Mechanical enhancement and weakening in Mo_6S_6 nanowire by twisting

Ke Xu(徐克), Yanwen Lin(林演文), Qiao Shi(石桥), Yuequn Fu(付越群), Yi Yang(杨毅), Zhisen Zhang(张志森), and Jianyang Wu(吴建洋)
Chin. Phys. B, 2023, 32 (**4**): 046204. DOI: 10.1088/1674-1056/aca7e7

Molecular dynamics study of coupled layer thickness and strain rate effect on tensile behaviors of Ti/Ni multilayered nanowires

Meng-Jia Su(宿梦嘉), Qiong Deng(邓琼), Lan-Ting Liu(刘兰亭), Lian-Yang Chen(陈连阳), Meng-Long Su(宿梦龙), and Min-Rong An(安敏荣)
Chin. Phys. B, 2021, 30 (**9**): 096201. DOI: 10.1088/1674-1056/abf10a

Mechanically tunable broadband terahertz modulator based on high-aligned Ni nanowire arrays

Wenfeng Xiang(相文峰), Xuan Liu(刘旋), Xiaowei Huang(黄晓炜), Qingli Zhou(周庆莉), Haizhong Guo(郭海中), and Songqing Zhao(赵嵩卿)
Chin. Phys. B, 2021, 30 (**2**): 026201. DOI: 10.1088/1674-1056/abd6f5

Proton radiation effect on GaAs/AlGaAs core-shell ensemble nanowires photo-detector

Li-Ying Tan(谭丽英), Fa-Jun Li(黎发军), Xiao-Long Xie(谢小龙), Yan-Ping Zhou(周彦平), Jing Ma(马晶)
Chin. Phys. B, 2017, 26 (**8**): 086202. DOI: 10.1088/1674-1056/26/8/086202

Study on irradiation-induced defects in GaAs/AlGaAs core-shell nanowires via photoluminescence technique

Li-Ying Tan(谭立英), Fa-Jun Li(黎发军), Xiao-Long Xie(谢小龙), Yan-Ping Zhou(周彦平), Jing Ma(马晶)
Chin. Phys. B, 2017, 26 (**8**): 086201. DOI: 10.1088/1674-1056/26/8/086201

Atomistic evaluation of tension–compression asymmetry in nanoscale body-centered-cubic AlCrFeCoNi high-entropy alloy

Runlong Xing(邢润龙) and Xuepeng Liu(刘雪鹏)†

Anhui Province Key Laboratory of Aerospace Structural Parts Forming Technology and Equipment, Institute of Industry and Equipment Technology, Hefei University of Technology, Hefei 230009, *China*

(Received 15 July 2023; revised manuscript received 20 September 2023; accepted manuscript online 22 September 2023)

The tension and compression of face-centered-cubic high-entropy alloy (HEA) nanowires are significantly asymmetric, but the tension–compression asymmetry in nanoscale body-centered-cubic (BCC) HEAs is still unclear. In this study, the tension–compression asymmetry of the BCC AlCrFeCoNi HEA nanowire is investigated using molecular dynamics simulations. The results show a significant asymmetry in both the yield and flow stresses, with BCC HEA nanowire stronger under compression than under tension. The strength asymmetry originates from the completely different deformation mechanisms in tension and compression. In compression, atomic amorphization dominates plastic deformation and contributes to the strengthening, while in tension, deformation twinning prevails and weakens the HEA nanowire. The tension–compression asymmetry exhibits a clear trend of increasing with the increasing nanowire cross-sectional edge length and decreasing temperature. In particular, the compressive strengths along the [001] and [111] crystallographic orientations are stronger than the tensile counterparts, while the [110] crystallographic orientation shows the exactly opposite trend. The dependences of tension–compression asymmetry on the cross-sectional edge length, crystallographic orientation, and temperature are explained in terms of the deformation behavior of HEA nanowire as well as its variations caused by the change in these influential factors. These findings may deepen our understanding of the tension–compression asymmetry of the BCC HEA nanowires.

Keywords: high-entropy alloys, body-centered-cubic, nanowire, tension–compression asymmetry, atomistic simulations

PACS: 62.25.–g, 62.23.Hj, 61.66.Dk, 02.70.Ns **DOI:** 10.1088/1674-1056/acfc37

1. Introduction

High-entropy alloys (HEAs) are a new class of solid-solution alloy systems that contain five or more principal elements in equimolar or near-equimolar concentrations, in which the proportion of each element is approximately between 5% and 35%.[1–3] This novel type of alloy exhibits four core effects, including high entropy, severe lattice distortion, sluggish diffusion, and cocktail effects.[4] Due to the high configurational entropy of mixing, HEAs have been found to form a simple solid solution phase instead of intermetallic phases. The crystal structure of HEAs can be face-centered cubic (FCC), body-centered cubic (BCC), hexagonal close-packed (HCP) or a mixture of these, depending on the content of constituent element.[5] HEAs usually possess more exceptional properties than traditional alloys, such as high strength and high ductility,[6,7] superior thermal stability,[8] and excellent resistance to irradiation,[9,10] wear,[11] and corrosion.[12] Because of their unique performances, HEAs have been widely applied in many advanced technology fields, such as hydrogen storage materials,[13] radiation resistant materials,[14] coating materials,[15] and aerospace industry.[16]

Among the numerous outstanding performances of HEAs, their mechanical performance is critically important for the engineer application and has attracted increasing attention in the past decade. A great number of experimental studies have been conducted to investigate the mechanical behavior and deformation mechanism of HEAs.[17,18] Ding *et al.*[19] revealed that tuning composition and element distribution can hinder the dislocation motion and thus enhance the mechanical properties of the CrMnFeCoNi HEAs. Gludovatz *et al.*[20] reported that a single-phase FCC CrMnFeCoNi HEA possesses excellent damage tolerance with tensile strengths exceeding 1 GPa and fracture toughness above 200 MPa·m$^{1/2}$, and the toughness of this HEA is greater than that of virtually all pure metals and metal alloys. Using in situ scanning electron microscope compression tests, Zhang and coauthors investigated the deformation behaviors and plastic mechanisms of CoCrFeNi[21] or AlCrFeCoNi[22] single crystals at the micro/nanoscale. They showed that the size and orientation of micro/nanopillars have a significant influence on the yield and flow stresses of HEAs. Zhao *et al.*[23] recently observed atomic amorphization in a CrMnFeCoNi HEA under severe plastic deformation, which provides an additional strengthening mechanism to enhance the capability of HEAs for extreme loading conditions. Additionally, the microstructures and mechanical properties of the HEAs can be also remarkably affected by the temperature[24] and strain rate.[25] Molecular dynamics (MD) simulation is a powerful atomic simulation approach to study the mechanical behaviors of HEAs, because it is capable of providing direct observations of the microstructure evolution during deformation process and unveiling the

†Corresponding author. E-mail: liuxuepeng@hfut.edu.cn

© 2024 Chinese Physical Society and IOP Publishing Ltd

microscopic deformation mechanism. In recent years, MD simulations were widely utilized to study the mechanical properties and deformation mechanisms of the HEAs. The predicted results from these MD simulations[26–32] can not only agree well with the experimental data but also reveal the new deformation mechanisms at microscale that is difficult to obtain in experiments.

Despite the remarkable progress in the studies of mechanical performances of HEAs, most of the investigations have concentrated on the mechanical properties of HEAs in one deformation path (such as tension or compression).[17–24,28–30] There has been little attention paid to the deformation behaviors of HEAs under both uniaxially tensile and compressive loadings. The vast majority of published literature report that the tension–compression asymmetry commonly exists in the nanoscale conventional metals and alloys[33–40] and inorganic composite materials.[41–44] As a novel type of metallic materials, research on the tension–compression asymmetry of HEAs is still in its initial stage. It is noteworthy that a recent experimental study[45] showed that an $Al_{0.3}$CrFeCoNi HEA nanowire with FCC phase exhibits an apparent asymmetry in work hardening behavior between tension and compression. Most recently, MD simulations indicated that an extraordinary tension–compression asymmetry was also observed in single crystal FCC[46] or amorphous/nanocrystalline composite[47] AlFeNiCrCu HEA nanowires. However, these studies are limited to the tension–compression asymmetry of FCC or amorphous HEA nanowires, and the understanding of the tension–compression asymmetry in nanoscale BCC HEAs is still obscure.

Motivated by the above reasons, we conduct atomistic MD simulations to study the mechanical behaviors of an AlCrFeCoNi HEA nanowire (a typical HEA with BCC structure) under both uniaxial tension and compression. The objective of this study is to examine and characterize the tension–compression asymmetry in nanoscale BCC AlCrFeCoNi HEAs and unveil the underlying microscopic mechanism of the observed asymmetric response. In particular, the influences of the nanowire cross-sectional edge length, crystallographic orientation, and temperature on the tension–compression asymmetry are systematically explored. This study is expected to not only deepen our insights into the tension–compression asymmetry of the nanoscale BCC HEAs but also provide guidance for the engineer application of BCC HEAs in the field of nanotechnology.

2. Computational methods

2.1. Interaction potential

In the current study, the interatomic interactions in BCC AlCrFeCoNi HEA nanowires are characterized utilizing the embedded-atom-method (EAM) potential proposed by Zhang *et al.*[22] The function expression of the EAM potential can be described by

$$E_i = F_\alpha\left(\sum_{j\neq i}\rho_\beta\left(r_{ij}\right)\right) + \frac{1}{2}\sum_{j\neq i}\varphi_{\alpha\beta}\left(r_{ij}\right), \tag{1}$$

in which F stands for the embedding energy, which is a function of the atomic electron density ρ. The term φ represents the pair potential energy, and r_{ij} is the separation between atoms i and j. The notations α and β are the element types of atoms i and j. The EAM potential has been recently used in MD simulations to investigate the plastic deformation mechanisms in single-crystalline BCC AlCrFeCoNi HEAs, and the simulation results are in good accordance with the experimental data.[22]

2.2. Preparation of BCC AlCrFeCoNi HEA nanowires

In this study, the BCC AlCrFeCoNi HEA nanowires with a square cross-section are considered. To construct the HEA nanowire, a BCC lattice is randomly occupied by Al, Cr, Fe, Co, Ni atoms with equimolar concentrations. In all simulation cells, lattice orientations of the BCC HEA nanowire are aligned along the [100], [010], and [001], except in Subsection 3.4 where the influence of crystallographic orientation of the nanowire axis direction is explored. The lattice parameter a is selected as 2.91 Å based on the experimental data.[22] The cross-sectional edge length d of the BCC HEA nanowire ranges from $30a$ to $90a$, and the axial length L of nanowire is obtained according to the fixed ratio of cross-sectional edge length to axial length of 1/3. The crystallographic orientations along the axis direction of BCC HEA nanowire are set as [001], [110], and [111] to consider the crystallographic orientation effect. Periodic boundary conditions are applied only along the axis direction of the nanowires, while free boundary conditions are imposed in other directions. After the initial structures are constructed, the energy of the BCC HEA nanowire is minimized. Then the nanowires are relaxed under the NPT ensemble (constant atom number, system pressure, and temperature) to for a long period until the system energy is typically converged. In the current research, the system temperature is allowed to vary from 300 K to 1200 K, and pressure is controlled at 0 GPa. The final equilibrated structure of a BCC AlCrFeCoNi HEA nanowire at 300 K is shown in Fig. 1(a), where the Al, Cr, Fe, Co, and Ni atoms are evenly distributed in the HEA nanowire. The AlCrFeCoNi HEA nanowire maintains the BCC structure after equilibration, which verifies that the atomic models constructed in this study are reasonable.

2.3. Simulation procedure of compression and tension tests

After relaxation, the BCC AlCrFeCoNi HEA nanowire is uniaxially stretched or compressed along the axial direction

of the nanowire with constant strain rates of $\pm 1.0 \times 10^9$, as schematically shown in Fig. 1(b). During the deformation, the canonical (NVT) ensemble is utilized to maintain a constant temperature. The stress and strain of the HEA sample are calculated by using the virial stress theorem.[48] All simulations in this work are performed using the classical parallel MD program LAMMPS.[49] The OVITO software[50] is used to visualize and analyze the simulation results. The common neighbor analysis (CNA) method[51] is used to identify the local crystal structure of the system, and the dislocations in the nanowire are extracted based on the dislocation extraction algorithm (DXA).[52]

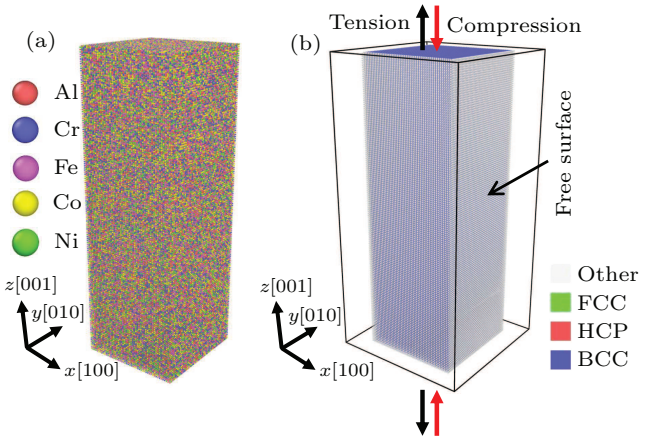


Fig. 1. (a) The relaxed structure of a BCC AlCrFeCoNi HEA nanowire with cross-sectional edge length of $d = 50a$ at 300 K. (b) The representative model of BCC AlCrFeCoNi HEA nanowire for uniaxial tension and compression tests, where the red arrows represent the compression direction and the black arrows stand for the tension direction. The model is colored according to the CNA pattern of atoms.

3. Results and discussion

3.1. The tension–compression asymmetry of BCC HEA nanowire

To study the tension–compression asymmetry of BCC AlCrFeCoNi HEA nanowire, an HEA sample with cross-sectional edge length of $50a$ is stretched and compressed along the [001] crystallographic orientation at temperature of 300 K. The tensile and compressive stress–strain curves of the HEA nanowire are depicted in Fig. 2(a). It is observed that there exist small fluctuations at initial stage of small strain in both the tensile and compressive stress–strain curves. Such a result can be attributed to the fact that some atomic bonds of atoms on the free surfaces of HEA nanowire are suspended. The thermal disturbance can easily destroy the balance of the surface atoms and cause violent atomic thermal motion, which results in a certain degree of stress perturbation. In order to quantify the tension–compression asymmetry, the peak stress in the yielding stage is taken as the yield stress of the HEA nanowire. Considering that the stress remains almost constant in the plastic flow stage, we thus select the stress at strain of 0.15 in the plateau region as the flow stress of the HEA nanowire for the sake of simplicity, according to the procedure reported in the previous literature.[22] It can be seen that both yield and flow stresses in compression are significantly larger than in tension for the AlCrFeCoNi HEA nanowire. Based on the work of Niu *et al.*[46] or Zhou *et al.*,[36] the tension–compression asymmetry for a metal or alloy nanowire can be quantitatively measured in terms of the ratio of compressive yield stress to tensile yield stress $\sigma_{\mathrm{Y}}^{\mathrm{C}}/\sigma_{\mathrm{Y}}^{\mathrm{T}}$ or the ratio of compressive flow stress to tensile flow stress $\sigma_{\mathrm{F}}^{\mathrm{C}}/\sigma_{\mathrm{F}}^{\mathrm{T}}$. The tension–compression asymmetry $\sigma_{\mathrm{Y}}^{\mathrm{C}}/\sigma_{\mathrm{Y}}^{\mathrm{T}}$ and $\sigma_{\mathrm{F}}^{\mathrm{C}}/\sigma_{\mathrm{F}}^{\mathrm{T}}$ of the BCC AlCrFeCoNi HEA nanowire are calculated to be 2.13 and 4.16, respectively. These observations clearly show that the BCC AlCrFeCoNi HEA nanowire exhibit a remarkable asymmetry in strength under tension and compression. It is interesting to note that a recent atomistic simulation study by Niu *et al.*[46] showed that the FCC Al_xFeNiCoCu HEA nanowire exhibits a completely opposite tension–compression strength asymmetry to the case of BCC AlCrFeCoNi HEA nanowire, i.e., its compressive strength is much lower than the tensile strength.

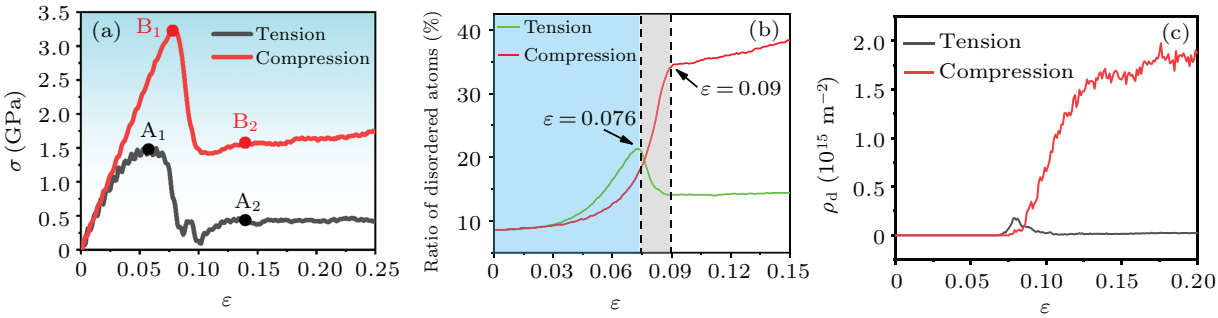


Fig. 2. (a) Tensile and compressive stress–strain curves of the BCC AlCrFeCoNi HEA nanowire with cross-sectional edge length of $d = 50a$ along the [001] crystallographic orientation at 300 K. (b) The ratio of disordered atoms to the total atoms of the HEA nanowire as a function of strain during the tension and compression process. (c) Variations of the dislocation densities (ρ_{d}) in the BCC AlCrFeCoNi HEA nanowire as a function of the strain during stretching and compressing.

To understand the strength asymmetry in tension and compression of BCC AlCrFeCoNi HEA nanowire, we take a closer look at the atomic structure evolution of the sample during tension and compression processes. We first analyze the deformation details in tension, and the local structural coordination (analyzed by CNA method) and dislocation activities

(analyzed by DXA analysis) of the HEA nanowire at several typical tensile strains are presented in Figs. 3(a)–3(c), respectively. Combining with the tensile stress–strain relationship illustrated in Fig. 2(a), it can be seen that the BCC AlCrFeCoNi HEA nanowire mainly undergoes three typical deformation stages during tension. In the first stage of small strain ($0 < \varepsilon < 0.059$), the stress–strain relationship obeys a linearly increased trend (see Fig. 2(a)). There is little phase transformation (see Fig. 3(a1)) and no dislocations (see Fig. 3(b1)) at this stage, which are typical characteristics of the linear-elastic regime. We note that a very small number of disordered atoms are also found to exist in the elastic deformation stage (see Fig. 3(a1)), which can be ascribed to the pronounced solid solution in HEA.[4,5] When the strain attains to 0.06 (point A_1 in Fig. 2(a)), the stress reaches peak value and then drops suddenly, which indicates that the HEA nanowire enters into the plastic yield regime. At this stage, the amounts of disordered atoms in the HEA nanowire continuously increases with the increasing strain (see Fig. 2(b)). In particular, dislocations begin to nucleate from the free surfaces at the strain of 0.069, as shown in Fig. 3(b3), and then several twin bands appear in the HEA nanowire at the strain of 0.075 (see Fig. 3(a3)). The twin formation mechanism is displayed in detail in Fig. 3(c). Firstly, the dislocations extend from surface to the interior by slipping on the specific slip planes (see Fig. 3(c1)) to generate the twin embryo (see Fig. 3(c2)). As the strain increases, the twin embryo gradually grows via the migration of twin boundary (see Fig. 3(c3)) and a twin band finally forms in the HEA nanowire (see Fig. 3(c4)). With the continuous loading, these twin bands have a certain degree of expansion (see Fig. 3(a4)). Obvious amorphization is concurrently occurred in the HEA nanowire during this period (see Fig. 3(a3)), but it quickly disappears with the expansion of twin bands (see Fig. 3(a4)), which can be also evidenced by the abruptly decreased number of disordered atoms in the green curve shown in Fig. 2(b). As the strain further increases to 0.13 (point A_2 in Fig. 2(a)), the tensile stress–strain curve shows serration flow behaviors and the stress remains essentially unchanged with the strain, implying that the BCC HEA nanowire enters into the plastic flow regime. With the increase of strain, twin bands gradually expand and are eventually intersected and overlapped with each other (see Figs. 3(a5) and 3(a6)), which dominates the deformation mechanism in the plastic flow regime. During the entire tension process, the dislocation activities are rather rare in the HEA nanowire and only a small amount of dislocation can be observed in the sample during plastic deformation (see Figs. 2(c) and 3(b3)–3(b6)).

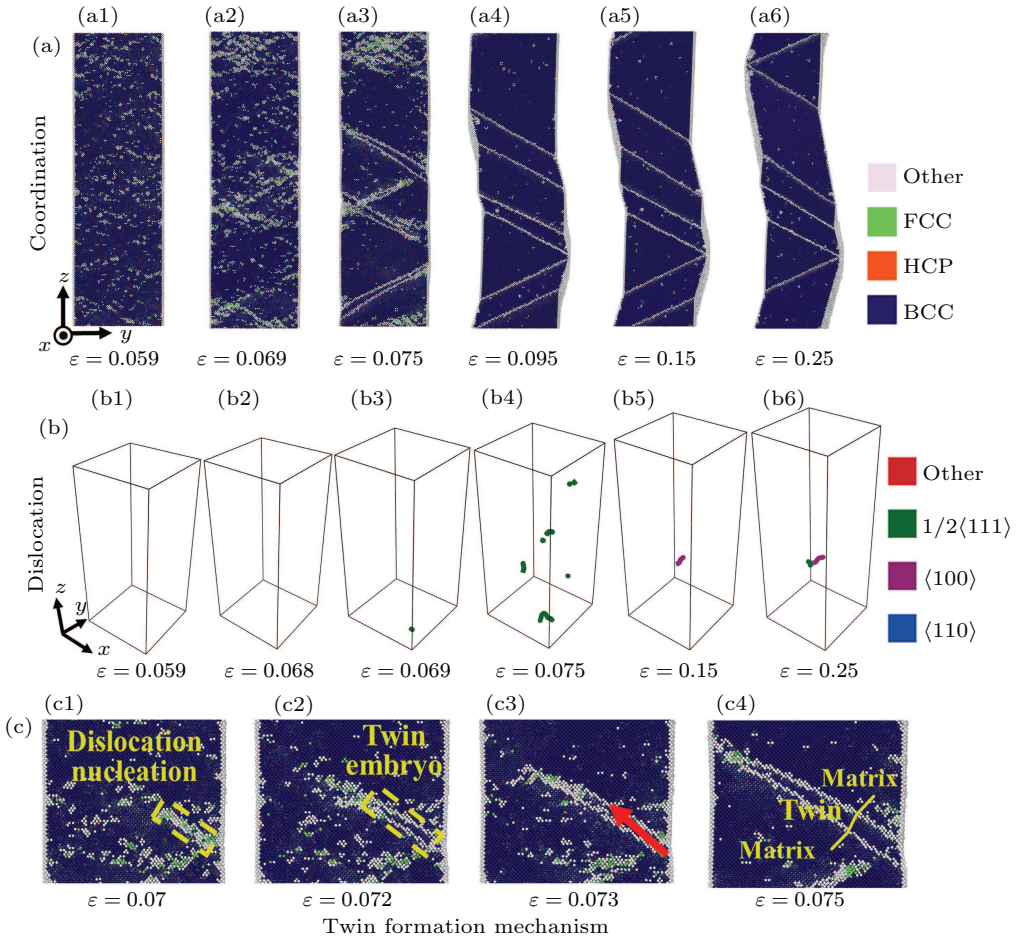


Fig. 3. (a) Atomic structure evolution and (b) dislocation activities of the BCC AlCrFeCoNi HEA nanowire with cross-sectional edge length of $d = 50a$ during stretching along the [001] crystallographic orientation at 300 K. (c) The twin formation mechanism during tension. The white, green, orange, and blue spheres in panels (a) and (c) represent the other, FCC, HCP, and BCC atoms, respectively.

Figures 4(a)–4(c) show the microstructure evolution and dislocation activities of the HEA nanowire during compression process, respectively. It can be seen that the BCC AlCrFeCoNi HEA nanowire also experiences three typical deformation regimes during compression, i.e., linear elastic, plastic yield, and plastic flow regime. In the linear elastic regime ($0 < \varepsilon < 0.075$), the stress increases linearly with the growing strain (see Fig. 2(a)), and no defect is observed in the HEA nanowire. After the linear elastic regime, the HEA nanowire sample starts to sustain plastic yielding at strain of 0.076 (point B_1 in Fig. 2(a)). At this stage, the stress decreases sharply within a narrow strain range, and dislocations constantly multiply and slip in the HEA nanowire with the increasing strain (see Figs. 4(b2) and 4(b3)). Subsequently, substantial amorphization occurs in the BCC HEA nanowire (see Figs. 4(a3) and 4(a4)). Quantitative dislocation density analysis shows that the amount of dislocations in the HEA under compression is remarkably larger than that in tension, as illustrated in Fig. 2(c). The formation mechanism of amorphous islands is shown in Fig. 4(c). Firstly, the dislocations slip on the specific slip planes induces some localized slip bands (see Fig. 4(c1)). Then numerous dislocations accumulate and tangle around the slip bands, which leads to the nucleation of amorphous islands (see Fig. 4(c2)). As the strain increases, the internal stress disorders the HEA around the amorphous phase and promotes the growth of amorphous islands (see Fig. 4(c3)), and finally a large area of amorphization appears ((see Fig. 4(c4))). It is clearly seen in Fig. 2(b) that the disordered atoms significantly increase during the plastic yield stage, which can also demonstrate the massive occurrence of amorphization in the HEA nanowire. Subsequently, the HEA sample enters into the plastic flow regime with the stress fluctuating over a small range, where the amorphous islands are constantly expanded in the nanowire (see Figs. 4(a5) and 4(a6)). We note that a recent experiment by Zhao *et al.*[23] showed that such amorphous islands were also observed in extreme deformation of the CrMnFeCoNi HEA.

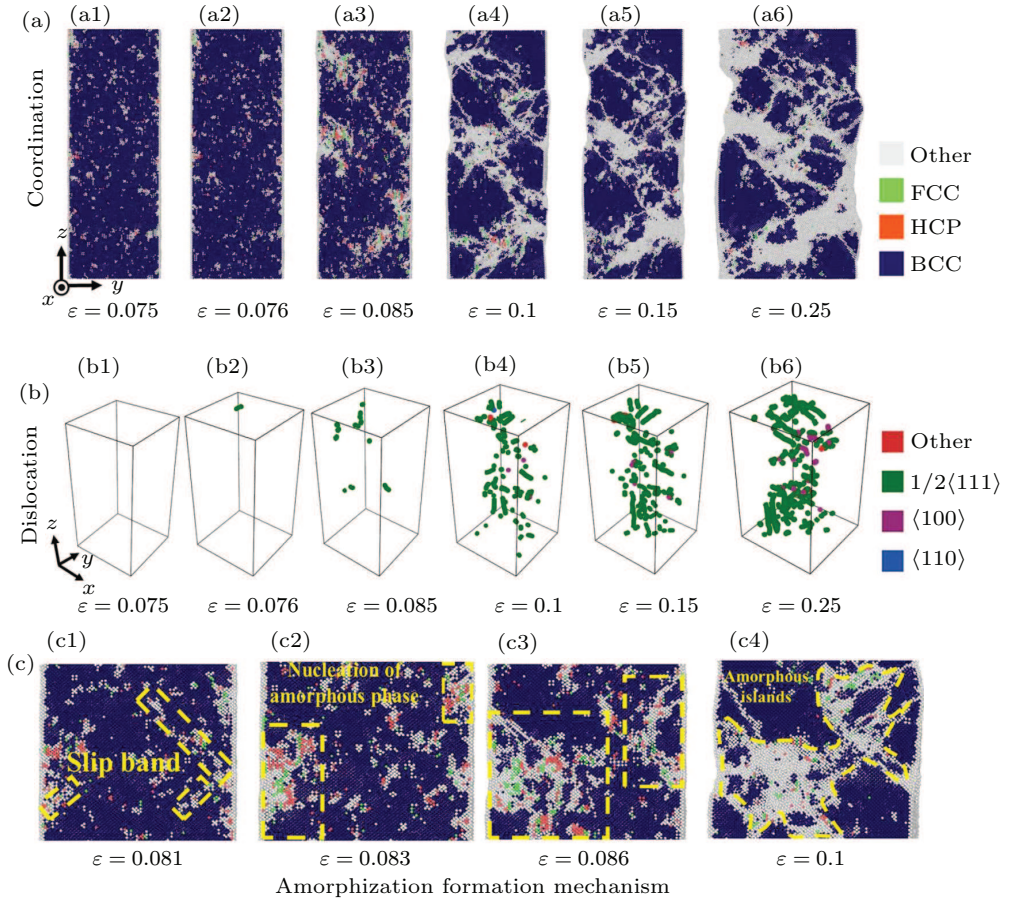


Fig. 4. (a) Atomic structure evolution and (b) dislocation activities of the BCC AlCrFeCoNi HEA nanowire with cross-sectional edge length of $d = 50a$ during compressing along the [001] crystallographic orientation at 300 K. (c) The amorphization formation mechanism during compression.

On the whole, it can be concluded that there is an apparent asymmetry between the deformation mechanisms of BCC AlCrFeCoNi HEA nanowire during tension and compression. Under tension, deformation twinning is the dominate plastic deformation mechanism of the nanowire. However, dislocation slip, tangling and accumulation, and atomic amorphization are the main plastic deformation events of BCC HEA nanowire during compression. During stretching, the de-

formation twinning weakens the nanowire and thus decreases the strength of the BCC HEA nanowire. While in compression, the amorphous islands can effectively hinder the slip and movement of dislocations[23,53,54] and thus enhance the strength of the nanowire. As a consequence, the strength of the BCC AlCrCoFeNi nanowire in compression is much stronger than that in tension.

3.2. Effect of nanowire cross-sectional edge length

To identify the influence of the nanowire cross-sectional edge length on the tension–compression asymmetry of nanoscale BCC HEA, simulations are performed for the BCC AlCrFeCoNi HEA nanowire with different cross-sectional edge lengths (from 30a to 90a) under tension and compression along the [001] crystallographic orientation at temperature of 300 K, and the stress–strain curves are illustrated in Figs. 5(a) and 5(b), respectively. It is observed that the tensile and compressive yield stresses both increase with the increasing edge length, which can be attributed to the size effect of HEA nanowire. As shown in Fig. 6(c), the atomic potential energy of surface atoms diminishes as the cross-sectional edge length of the nanowire increases. The increased atomic potential energy leads to the enhanced energy barrier for the dislocation and twin formation, which makes it more difficult for the occurrence of plastic deformation and thus causes an increased yield stress. In addition, it can be also seen that the Young's moduli in tension and compression both reduce with the decreasing cross-sectional edge length. The reduction in Young's modulus of BCC HEAs with the decreasing cross-sectional edge length can be ascribed to the size effect. A surface Young's modulus can be defined for the surface region of HEA nanowire with nanoscale depth, which has a lower value than the bulk Young's modulus.[55] The overall Young's modulus of HEA nanowire is the weighted average of the bulk modulus and the surface modulus with the respective thickness as weight factor. With the decrease of cross-sectional edge length, the surface-to-volume ratio increases and hence leads to a reduced Young's modulus. We note that the previous experimental observations[55–57] also showed the Young's modulus of silicon nanowire or nanoplate decreases monotonously as the specimen becomes thinner. The compressive flow stress is found to increase with the enlarging edge length, while the tensile flow stress is essentially independent on the edge length. Figures 5(c) and 5(d) present the variations of the tension–compression asymmetry $\sigma_{\mathrm{Y}}^{\mathrm{C}}/\sigma_{\mathrm{Y}}^{\mathrm{T}}$ and $\sigma_{\mathrm{F}}^{\mathrm{C}}/\sigma_{\mathrm{F}}^{\mathrm{T}}$ for the BCC AlCrFeCoNi HEA nanowire with cross-sectional edge length increasing from 30a to 90a, respectively. It is notable that both $\sigma_{\mathrm{Y}}^{\mathrm{C}}/\sigma_{\mathrm{Y}}^{\mathrm{T}}$ and $\sigma_{\mathrm{F}}^{\mathrm{C}}/\sigma_{\mathrm{F}}^{\mathrm{T}}$ exhibit an obvious trend of increasing with the increasing edge length, which indicates that increased degree of compressive strength is larger than that of tensile strength as the edge length increases.

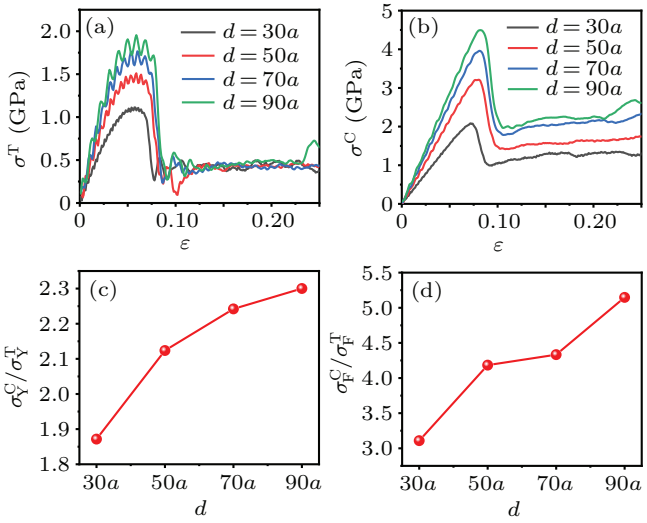


Fig. 5. Mechanical properties of the BCC AlCrFeCoNi HEA nanowire with different cross-sectional edge lengths along the [001] crystallographic orientation at 300 K: (a) tensile stress–strain curves; (b) compressive stress–strain curves; tension–compression asymmetry (c) $\sigma_{\mathrm{Y}}^{\mathrm{C}}/\sigma_{\mathrm{Y}}^{\mathrm{T}}$ and (d) $\sigma_{\mathrm{F}}^{\mathrm{C}}/\sigma_{\mathrm{F}}^{\mathrm{T}}$.

To understand the effect of nanowire cross-sectional edge length on the tension–compression asymmetry, the atomic structures of the BCC AlCrFeCoNi HEA nanowire with various cross-sectional edge lengths during tension and compression at a typical strain of $\varepsilon = 0.1$ are analyzed and displayed in Figs. 6(a) and 6(b), respectively. It can be seen from Fig. 6(a) that the number of twin bands markedly increases with the increasing edge length of the HEA nanowire during stretching. The increased number of twin bands weakens the HEA nanowire and thus slows down the enhancement of tensile strength as the edge length of nanowire increases. Under compression, it is observed that the degree of amorphization in the BCC HEA nanowire significantly expands with the increasing edge length (see Fig. 6(b)). Such a scenario can be also evidenced by the increased proportion of disordered atoms in the HEA nanowire with the longer cross-sectional edge length during compression, as shown in Fig. 6(d). The more amorphization increases the resistance of the dislocation slip during compression, which speeds up the increase of compressive strength as the cross-sectional edge length of HEA nanowire becomes longer. To sum up, increasing cross-sectional edge length of the BCC AlCrFeCoNi HEA nanowire promotes the twin formation during stretching, which slows down the enhancement of tensile strength. While compressing, the increase of edge length contributes to the amorphization, which increases the resistance of dislocation slip in the HEA nanowire and thus speeds up the increase of compressive strength. As a result, with the increase of cross-sectional edge length, the increased degree of compressive strength is larger than that of tensile strength, so that the tension–compression asymmetry of BCC AlCrFeCoNi HEA nanowire increases.

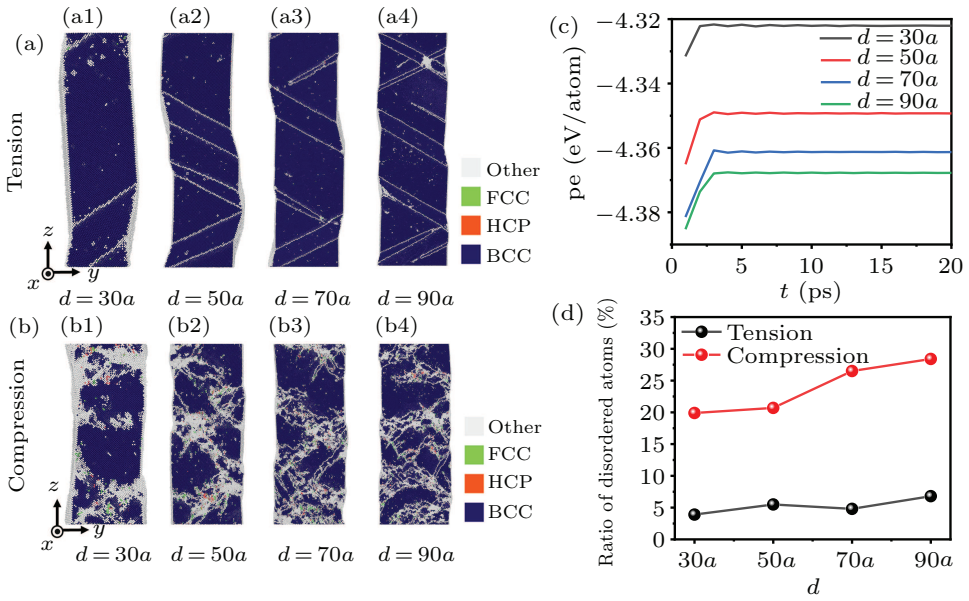


Fig. 6. The atomic structures of the BCC AlCrFeCoNi HEA nanowire with different cross-sectional edge lengths along the [001] crystallographic orientation at 300 K during (a) stretching and (b) compressing at strain of $\varepsilon = 0.1$. (c) The potential energy (pe) per atom in BCC AlCrFeCoNi HEA nanowire with various cross-sectional edge lengths during relaxation at 300 K. (d) The ratio of disordered atoms to the total atoms of the HEA nanowire with various cross-sectional edge lengths at strain of $\varepsilon = 0.1$ under tension and compression.

3.3. Effect of temperature

To examine the influence of the temperature on the tension–compression asymmetry of the BCC AlCrFeCoNi HEA nanowire, simulations are performed for the HEA sample with cross-sectional edge length of $50a$ during stretching and compressing along the [001] crystallographic orientation at a wide range of temperature from 300 K to 1200 K. Figures 7(a) and 7(b) display the tensile and compressive stress–strain curves of the BCC AlCrCoFeNi HEA nanowire at 300 K, 600 K, 900 K, and 1200 K, respectively. It can be seen that the yield stress and Young's modulus in tension or compression both decrease as the temperature rises. Such a result can be attributed to the more violent thermal motion of atoms at higher temperature. The stronger atomic thermal movement results in a weaker bond between the atoms in the HEA nanowire, so that the sample is more vulnerable to the deformation and hence causes the lower yield stress and Young's modulus. The temperature has a remarkable impact on the tension–compression asymmetry of the BCC AlCrCoFeNi HEA nanowire. As seen from Figs. 7(c) and 7(d), the tension–compression asymmetry $\sigma_{\mathrm{Y}}^{\mathrm{C}}/\sigma_{\mathrm{Y}}^{\mathrm{T}}$ and $\sigma_{\mathrm{F}}^{\mathrm{C}}/\sigma_{\mathrm{F}}^{\mathrm{T}}$ both reduce with the increasing temperature, implying that decreased degree of compressive strength is larger than that of tensile strength as the temperature rises.

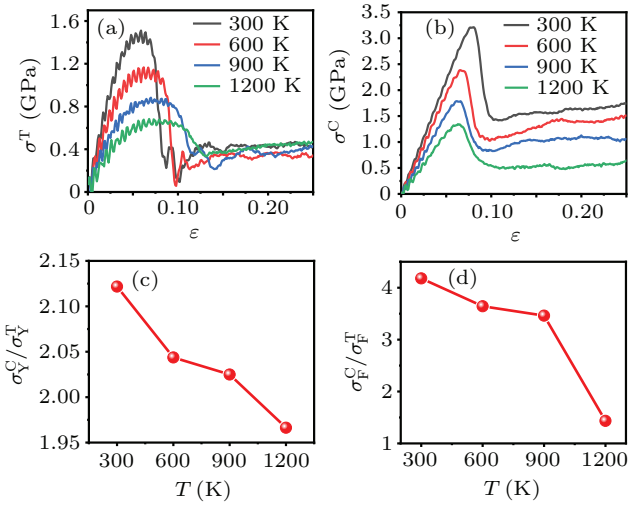


Fig. 7. Mechanical properties of the BCC AlCrFeCoNi HEA nanowire with cross-sectional edge length of $50a$ during stretching and compressing along the [001] crystallographic orientation at different temperatures: (a) tensile stress–strain curves; (b) compressive stress–strain curves; tension–compression asymmetry (c) $\sigma_{\mathrm{Y}}^{\mathrm{C}}/\sigma_{\mathrm{Y}}^{\mathrm{T}}$ and (d) $\sigma_{\mathrm{F}}^{\mathrm{C}}/\sigma_{\mathrm{F}}^{\mathrm{T}}$.

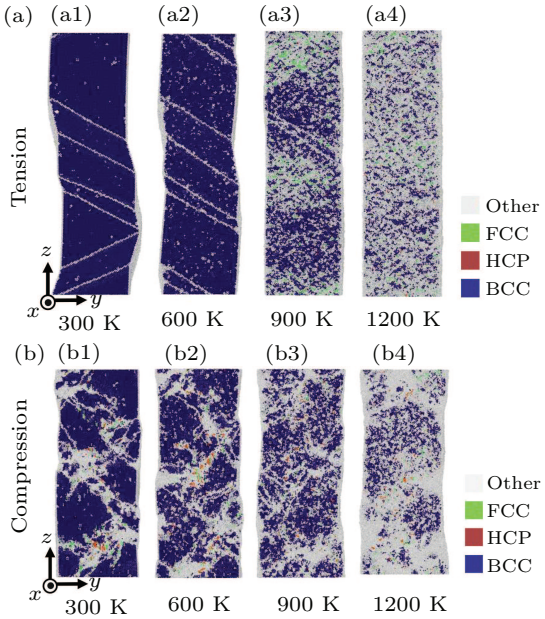


Fig. 8. The atomic structures of the BCC AlCrFeCoNi HEA nanowire with cross-sectional edge length of $50a$ along the [001] crystallographic orientation at different temperatures during (a) stretching and (b) compressing at strain of $\varepsilon = 0.1$.

To understand the temperature effect on the tension–compression asymmetry, the microstructures of the BCC AlCrFeCoNi HEA nanowire during deformation at a typical strain of $\varepsilon = 0.1$ under different temperature conditions are analyzed and presented in Figs. 8(a) and 8(b), respectively. It is observed that with the increase of temperature, the atomic thermal motion in the HEA nanowire tends to be more violent, and more disordered atoms are generated in the HEA nanowire. In particular, we observed that a vast majority of amorphous atoms are randomly distributed in the HEA nanowire during tension and compression at high temperatures of 900 (see Figs. 8(a3) and 8(b3)) or 1200 K (see Figs. 8(a4) and 8(b4)). These disordered atoms can remarkably suppress the twin formation and dislocation activities in the HEA nanowire during deformation. On the one hand, it can be seen that the twin bands in the HEA nanowire during stretching are easily disrupted by the thermal disturbance (see Fig. 8(a3)) and hard to form at high temperature (see Fig. 8(a4)). The less formation of twin contributes to the strengthening and thus slows down the reduction of tensile strength as the temperature increases. On the other hand, thermal disturbance is also able to disturb the amorphous islands during compressing (see Fig. 8(b)) and the amorphous region becomes blurred at high temperature (see Fig. 8(b4)). Considering that the amorphous islands can effectively obstruct the slip and movement of dislocations and contributes to the strengthening,[23,53,54] the less amorphous islands at higher temperature diminishes the resistance of the dislocation slip so that the decrease of compressive strength is speeded up. The two factors in combination result in that the decreased degree of the compressive strength is larger than that of the tensile strength as the temperature increases, that is, the tension–compression asymmetry decreases.

3.4. Effect of crystallographic orientation

To explore the role of the crystallographic orientation on the tension–compression asymmetry of the BCC AlCrFeCoNi HEA nanowire, simulations are conducted for the sample with edge length of 50a during stretching and compressing along the [001], [110], and [111] crystallographic orientations at temperature of 300 K. The tensile and compressive stress–strain curves of the HEA sample deformed along the [001], [111], and [110] orientations are shown in Figs. 9(a)–9(c), respectively. For each crystallographic orientation, the tensile and compressive mechanical properties of the BCC AlCrFeCoNi HEA nanowire are apparently asymmetric. The yield and flow stresses are extracted from Figs. 9(a)–9(c), and the tension–compression asymmetry $\sigma_{\mathrm{Y}}^{\mathrm{C}}/\sigma_{\mathrm{Y}}^{\mathrm{T}}$ and $\sigma_{\mathrm{F}}^{\mathrm{C}}/\sigma_{\mathrm{F}}^{\mathrm{T}}$ along different crystallographic orientations are calculated, as illustrated in Table 1. It can be seen that there is a strong dependence between the tension–compression asymmetry and crystallographic orientation. The values of $\sigma_{\mathrm{Y}}^{\mathrm{C}}/\sigma_{\mathrm{Y}}^{\mathrm{T}}$ along the [001] and [111] crystallographic orientations are both significantly larger than 1, while that along the [110] orientation is less than 1. Similar conclusions can be also drawn for the ratio of $\sigma_{\mathrm{F}}^{\mathrm{C}}/\sigma_{\mathrm{F}}^{\mathrm{T}}$. This implies that the compressive strength is stronger than the tensile counterpart as the BCC AlCrFeCoNi HEA nanowire deformed along the [001] and [111] crystallographic orientations. In contrast, during deformation along the [110] orientations, the compressive strength is smaller than the tensile strength.

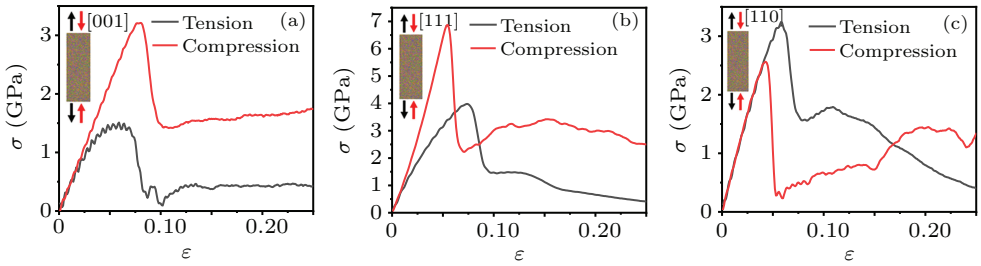


Fig. 9. Tensile and compressive stress–strain curves of the BCC AlCrFeCoNi HEA nanowire with cross-sectional edge length of 50a along the (a) [001], (b) [111], and (c) [110] crystallographic orientations at 300 K.

Table 1. The tension–compression asymmetry of the BCC AlCrFeCoNi HEA nanowire with cross-sectional edge length of 50a along [001], [111], and [110] crystallographic orientations during stretching and compressing at 300 K.

	[001]	[111]	[110]
$\sigma_{\mathrm{Y}}^{\mathrm{C}}$ (GPa)	3.21	6.87	2.56
$\sigma_{\mathrm{Y}}^{\mathrm{T}}$ (GPa)	1.51	3.98	3.24
$\sigma_{\mathrm{Y}}^{\mathrm{C}}/\sigma_{\mathrm{Y}}^{\mathrm{T}}$	2.13	1.73	0.79
$\sigma_{\mathrm{F}}^{\mathrm{C}}$ (GPa)	1.58	3.40	0.72
$\sigma_{\mathrm{F}}^{\mathrm{T}}$ (GPa)	0.38	1.12	1.44
$\sigma_{\mathrm{F}}^{\mathrm{C}}/\sigma_{\mathrm{F}}^{\mathrm{T}}$	4.16	3.04	0.50

To understand the impact of crystallographic orientation on the tension–compression asymmetry, the atomic structures of the BCC AlCrFeCoNi HEA nanowire during stretching and compressing along various crystallographic orientations at some typical strains are analyzed, as displayed in Figs. 10(a) and 10(b). It can be seen that the deformation mechanism of the BCC AlCrFeCoNi HEA nanowire is remarkably impacted by the crystallographic orientation. In the case of [001] crystallographic orientation, twinning is the primary deformation mechanism during stretching (see Fig. 10(a1)) while atomic amorphization dominates the plastic deformation of the HEA nanowire in compression (see Fig. 10(b1)). The amorphization

facilitates the strengthening of the BCC AlCrCoFeNi HEA nanowire but deformation twinning leads to the weakening, so that the compressive mechanical properties of the [001] crystallographic orientation are more robust than the tensile counterparts. For the [111] crystallographic orientation, it is observed that dislocation slip forms multiple slip bands in the [111]-oriented nanowire during stretching (see Fig. 10(a2)), thus reducing the strength of the HEA nanowire. Compression along the [111] orientation leads to the production of numerous small-sized amorphous islands in the nanowire (see Fig. 10(b2)).

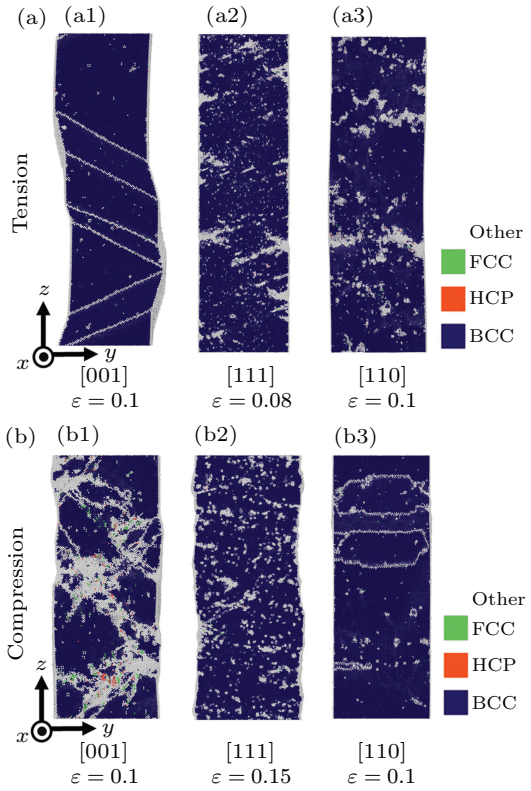


Fig. 10. The atomic structure evolutions of the BCC AlCrFeCoNi HEA nanowire with cross-sectional edge length of 50a along [001], [111], and [110] crystallographic orientations during (a) stretching and (b) compressing.

These numerous small-sized amorphous islands significantly resist the dislocation slip and contribute to the strengthening, which results in a higher compressive strength. Therefore, the compressive strength of the [111] crystallographic orientation is larger than the tensile strength. However, when stretching along the [110] crystalline orientation, dislocations nucleate from the free surface of the HEA nanowire and travel inside the nanowire, which results in the obvious amorphization in the HEA nanowire (see Fig. 10(a3)) and thus enhances the strength of the nanowire. In contrast to the [001] and [111] crystallographic orientations, compressing along the [110] crystalline orientation leaves abundant twins in the HEA nanowire (see Fig. 10(b3)), thus reducing the strength of the nanowire. Consequently, the tensile strength is greater than the compressive strength when the BCC AlCrFeCoNi HEA nanowire deformed along the [110] crystallographic orientation, which shows the opposite trend to the cases of [001] and [111] orientations.

4. Conclusions

In summary, we have performed atomistic MD simulations to study the tension–compression asymmetry of BCC AlCrFeCoNi HEA nanowires, and its dependences on the nanowire cross-sectional edge length, crystallographic orientation, and temperature were systematically analyzed. The main conclusions are as follows:

(i) The BCC AlCrFeCoNi HEA nanowire exhibits an obvious tension–compression asymmetry with yield and flow stresses in compression both significantly larger than those in tension, which mainly due to the completely different deformation mechanisms under tensile and compressive loadings. During stretching, deformation twinning dominates plastic deformation and weakens the HEA nanowire. While compressing, dislocation slip, tangling, and accumulation produce substantial amorphization that can effectively resist the dislocation slip and contribute to the strengthening.

(ii) Increasing cross-sectional edge length of the HEA nanowire promotes the deformation twinning in tension and facilitates the amorphization in compression, which results in the increased tension–compression asymmetry.

(iii) The increase of temperature leads to more disordered atoms in the BCC HEA nanowire. These disordered atoms can remarkably suppress the deformation twinning during stretching and amorphization during compressing, causing the tension–compression asymmetry to reduce with the raising temperature.

(iv) The tension–compression asymmetry of BCC AlCrFeCoNi HEA nanowire is highly dependent on the crystallographic orientation. The compressive strength along the [001] and [111] crystallographic orientations is stronger than the tensile counterpart, while the [110] crystallographic orientation presents the completely opposite trend. When loading along the [110] crystallographic orientation, amorphization is a controlling deformation mechanism in tension and strengthens the nanowire, while deformation twinning dominates the compressive deformation mechanism and weakens the nanowire, so that the compressive strength is weaker than the tensile strength.

Acknowledgements

Project supported by the National Natural Science Foundation of China (Grant No. 12272118) and the National Key Research and Development Program of China (Grant No. 2022YFE03030003).

References

[1] Yeh J W, Chen S K, Lin S J, Gan J Y, Chin T S, Shun T T, Tsau C H and Chang S Y 2004 *Adv. Eng. Mater.* **6** 299

[2] Cao G, Liang J, Guo Z, Yang K, Wang G, Wang H L, Wan X, Li Z, Bai Y, Zhang Y, Liu J, Feng Y, Zheng Z, Lu, He G, Xiong Z, Liu Z, Chen S, Guo Y, Zeng M, Lin J and Fu L 2023 *Nature* **619** 73

[3] Liu Y, Ren J, Guan S, Li C, Zhang Y, Muskeri S, Liu Z, Yu D, Chen Y, An K, Cao Y, Liu W, Zhu Y, Chen W, Mukherjee S, Zhu T and Chen W 2023 *Acta Mater.* **250** 118884

[4] Tsai M H and Yeh J W 2014 *Mater. Res. Lett.* **2** 107

[5] George E P, Raabe D and Ritchie R O 2019 *Nat. Rev. Mater.* **4** 515

[6] Lei Z, Liu X, Wu Y, Wang H, Jiang S, Wang S, Hui X, Wu Y, Gault B, Kontis P, Raabe D, Gu L, Zhang Q, Chen H, Wang H, Liu J, An K, Zeng Q, Nieh T G and Lu Z 2018 *Nature* **563** 546

[7] Chen S, Aitken Z H, Pattamatta S, Wu Z, Yu Z G, Srolovitz D J, Liaw P K and Zhang Y W 2021 *Nat. Commun.* **12** 4953

[8] Karati A, Guruvidyathri K, Hariharan V S and Murty B S 2019 *Scr. Mater.* **162** 465

[9] El-Atwani O, Li N, Li M, Devaraj A, Baldwin J K S, Schneider M M, Sobieraj D, Wróbel J S, Nguyen-Manh D, Maloy S A and Martinez E 2019 *Sci. Adv.* **5** eaav2002

[10] El-Atwani O, Vo H T, Tunes M A, Lee C, Alvarado A, Krienke N, Poplawsky J D, Kohnert A A, Gigax J, Chen W Y, Li M, Wang Y Q, Wróbel J S, Nguyen-Manh D, Baldwin J K S, Tukac O U, Aydogan E, Fensin S and Martinez E 2023 *Nat. Commun.* **14** 2516

[11] Verma A, Tarate P, Abhyankar A C, Mohape M R, Gowtam D S, Deshmukh V P and Shanmugasundaram T 2019 *Scr. Mater.* **161** 28

[12] Fu Y, Li J, Luo H, Du C and Li X 2021 *J. Mater. Sci. Technol.* **80** 217

[13] Kao Y F, Chen S K, Sheu J H, Lin J T, Lin W E, Yeh J W, Lin S J, Liou T H and Wang C W 2010 *Int. J. Hydrogen Energy* **35** 9046

[14] Zhang Y, Zuo T T, Tang Z, Gao M C, Dahmen K A, Liaw P K and Lu Z P 2014 *Prog. Mater. Sci.* **61** 1

[15] He C Y, Gao X H, Yu D M, Zhao S S, Guo H X and Liu G 2021 *J. Mater. Chem. A* **9** 21270

[16] Postolnyi B, Buranich V, Smyrnova K, Araújo J P, Rebouta L, Pogrebnjak A and Rogoz V 2021 *IOP Conf. Ser.: Mater. Sci. Eng.* **1024** 012009

[17] George E P, Curtin W A and Tasan C C 2020 *Acta Mater.* **188** 435

[18] Li W, Xie D, Li D, Zhang Y, Gao Y and Liaw P K 2021 *Prog. Mater. Sci.* **118** 100777

[19] Ding Q, Zhang Y, Chen X, Fu X, Chen D, Chen S, Gu L, Wei F, Bei H, Gao Y, Wen M, Li J, Zhang Z, Zhu T, Ritchie R O and Yu Q 2019 *Nature* **574** 223

[20] Gludovatz B, Hohenwarter A, Catoor D, Chang E H, George E P and Ritchie R O 2014 *Science* **345** 1153

[21] Zhang Q, Huang R, Jiang J, Cao T, Zeng Y, Li J, Xue Y and Li X 2022 *J. Mech. Phys. Solids* **162** 104853

[22] Zhang Q, Huang R, Zhang X, Cao T, Xue Y and Li X 2021 *Nano Lett.* **21** 3671

[23] Zhao S, Li Z, Zhu C, Yang W, Zhang Z, Armstrong D E J, Grant P S, Ritchie R O and Meyers M A 2021 *Sci. Adv.* **7** eabb3108

[24] Otto F, Dlouhy A, Somsen C, Bei H, Eggeler G and George E P 2013 *Acta Mater.* **61** 5743

[25] Wang L, Qiao J W, Ma S G, Jiao Z M, Zhang T W, Chen G, Zhao D, Zhang Y and Wang Z H 2018 *Mater. Sci. Eng. A* **727** 208

[26] Tang Y and Li D Y 2022 *Sci. Adv.* **8** eabp9096

[27] Yin S, Zuo Y, Abu-Odeh A, Zheng H, Li X G, Ding J, Ong S P, Asta M and Ritchie R O 2021 *Nat. Commun.* **12** 4873

[28] Zheng T, Lv J, Wu Y, Wu H H, Liu S, Tang J, Zhou M, Wang H, Liu X, Jiang S and Lu Z 2021 *Appl. Phys. Lett.* **119** 201907

[29] Gao T, Song H, Wang B, Gao Y, Liu Y, Xie Q, Chen Q, Xiao Q and Liang Y 2023 *Int. J. Mech. Sci.* **237** 107800

[30] Shen T Z, Song H Y, An M R and Li Y L 2022 *J. Appl. Phys.* **131** 094304

[31] Qi Y, He T and Feng M 2021 *J. Appl. Phys.* **129** 195104

[32] Tian Y, Fang Q and Li J 2020 *Nanotechnology* **31** 465701

[33] Xu Z, Li G, Zhou Y, Guo C, Huang Y, Hu X, Li X and Zhu Q 2023 *J. Alloys Compd.* **945** 169313

[34] Zhang D, Liu X, Li T, Fu K, Peng Z and Zhu Y 2022 *Comput. Mater. Sci.* **208** 111360

[35] Long J, Pan Q, Tao N and Lu L 2018 *Mater. Res. Lett.* **6** 456

[36] Zhou K, Liu B, Shao S and Yao Y 2017 *Phys. Lett. A* **381** 1163

[37] Tschopp M A and McDowell D L 2007 *Appl. Phys. Lett.* **90** 121916

[38] Park H S, Gall K and Zimmerman J A 2006 *J. Mech. Phys. Solids* **54** 1862

[39] Monk J and Farkas D 2007 *Philos. Mag.* **87** 2233

[40] Lund A C, Nieh T G and Schuh C A 2004 *Phys. Rev. B* **69** 012101

[41] Wang Y, Ding J, Fan Z, Tian L, Li M, Lu H, Zhang Y, Ma E, Li J and Shan Z 2021 *Nat. Mater.* **20** 1371

[42] Burg J A and Dauskardt R H 2016 *Nat. Mater.* **15** 974

[43] Liu X, Xu K, Ni Y, Lu P, Wang G and He L 2022 *J. Appl. Phys.* **132** 075104

[44] Yin B B, Sun W K, Zhang Y and Liew K M 2023 *Comput. Methods Appl. Mech. Eng.* **403** 115739

[45] Joseph J, Stanford N, Hodgson P and Fabijanic D M 2017 *Scr. Mater.* **129** 30

[46] Niu Y, Zhao D, Zhu B, Wang S, Wang Z and Zhao H 2022 *Nanotechnology* **33** 415703

[47] Niu Y, Zhao D, Zhu B, Wang S, Wang Z and Zhao H 2022 *Nanotechnology* **33** 105705

[48] Zimmerman J A, Webb III E B, Hoyt J J, Jones R E, Klein P A and Bammann D J 2004 *Modelling Simul. Mater. Sci. Eng.* **12** S319

[49] Plimpton S 1995 *J. Comput. Phys.* **117** 1

[50] Stukowski A 2010 *Modelling Simul. Mater. Sci. Eng.* **18** 015012

[51] Honeycutt J D and Anderson H C 1987 *J. Phys. Chem.* **91** 4950

[52] Stukowski A, Bulatov V V and Arsenlis A 2012 *Modelling Simul. Mater. Sci. Eng.* **20** 085007

[53] Fu Z, Jiang L, Waidini J L, MacDonlad B E, Wen H, Xiong W, Zhang D, Zhou Y, Rupert T J, Chen W and Lavermia E J 2018 *Sci. Adv.* **4** eaat8712

[54] Peng S, Wei Y and Gao H 2020 *Proc. Natl. Acad. Sci. USA* **117** 5204

[55] Li X, Ono T, Wang Y and Esashi M 2003 *Appl. Phys. Lett.* **83** 3081

[56] Wang J, Huang Q A and Yu H 2008 *J. Phys. D: Appl. Phys.* **41** 165406

[57] Broughton J Q, Meli C A, Vashishta P and Kalia R K 1997 *Phys. Rev. B* **56** 611